High temperature nano-indentation of tungsten: modelling and experimental validation

Xiazi Xiao[a*], D. Terentyev[b*], A. Ruiz[c], A. Zinovev[b,d], A. Bakaev[b], E. E. Zhurkin[e]

[a]Department of Mechanics, School of Civil Engineering, Central South University, Changsha 410075, P. R. China

[b]SCK•CEN, Nuclear Materials Science Institute, Boeretang 200, 2400 Mol, Belgium

[c]European Commission, DG Joint Research Centre, Nuclear Safety and Security Directorate. Westerduinweg 3, 1755LE Petten, The Netherlands.

[d]iMMC, Université catholique de Louvain, Av. Georges Lemaître 4, 1348 Louvain-la-Neuve, Belgium

[e]Department of Experimental Nuclear Physics K-89, Faculty of Physics and Mechanics, St.Petersburg State Polytechnical University, 29 Polytekhnicheskaya str., 195251, St.Petersburg, Russia

xxz2017@csu.edu.cn

dterenty@sckcen.be

[*]Corresponding authors.

Abstract

It is very well known that tungsten is intrinsically brittle at room temperature, and the characterization of its ductile properties by conventional mechanical tests is possible only above the ductile-to-brittle transition temperature (DBTT), i.e. above 500-700 K. However, the design of tungsten-based components often requires the knowledge of constitutive laws below the DBTT. Here, we carried out instrumented hardness measurements in the temperature range of 300-691 K by nano-indentation. The obtained results are used to extend a set of constitutive laws for the plastic deformation of tungsten, developed earlier on the basis of tensile data, which now covers the temperature range of 300-1273 K. The validation of the constitutive laws was realized by the crystal plasticity finite element method (CPFEM) model, which was applied to simulate the nano-indentation loading curves. The distribution of stress and strain under the indenter was also studied by the CPFEM to bring an insight on the extension of the plastic zone in the process of the

indentation, which is of crucial importance when nano-indentation is used to resolve the microstructural features generated by e.g. irradiation by energetic particles, plasma exposure or thermo-mechanical treatment.

Keywords: CPFEM, tungsten, dislocations, Hall-Petch

1. Introduction

Tungsten is one of the important materials for high-temperature applications such as shielding, armour or heating element in space applications, particle accelerators, furnaces and plasma-operating devices. Thanks to its high strength, thermal conductivity and melting point, tungsten is selected as the plasma-facing material in the world's largest fusion device under construction – ITER [1, 2]. Tungsten will protect the functional components, required to extract the fusion power, and therefore it will be subject to cyclic thermo-mechanical stresses originating from the plasma discharge. The mechanical and microstructural properties of the sub-surface region of the plasma-facing material will play a crucial role in its performance [3]. Although tungsten exhibits extremely high strength, bulk tungsten suffers from intrinsic brittleness, as its ductile-to-brittle transition temperature (DBTT) is around 500-700 K [4], which depends on the particular microstructure and composition (i.e. on the initial purity, fabrication route and final heat treatment). The onset of ductility appears to be controlled by the dislocation mobility and microstructural features limiting their multiplication and recombination. As a result of the extended operation in the fusion environment, the thermo-mechanical properties of the plasma facing material will degrade due to the repetitive thermal shocks (thermal cyclic fatigue), penetration of hydrogen isotopes (hydrogen embrittlement) and accumulation of irradiation damage (atomic collision cascades due to 14 MeV neutrons). Overall, the initially high DBTT will increase even further prompting a risk of cracking directly under operation [5]. The latter must be avoided to prevent the so-called loss of vacuum accident. As it was studied recently, the exposure to the high flux plasma and thermal shocks generates the strong damage pattern but in rather thin sub-surface layer (up to ~10 µm) [6-8]. This is why the understanding of the mechanical properties of rather thin regions of tungsten is of essential importance for the design of the plasma facing components. In addition, the usage of heavy ion irradiation is a common practice to simulate the neutron irradiation damage, but such method generates very shallow damage deposition profile (typically limited to 1-2 µm), so that conventional means of mechanical characterization cannot be applied [9-11].

The emergence of precise nano-scale experimental techniques such as nano-indentation (NI) and physically robust computational models has promoted a growing interest for the investigation of material sub-surface regions at nano- and atomic-scales (see e.g. [12-14] as what concerns tungsten). It has already been demonstrated that NI can be successfully used to characterize the impact of heavy ion irradiation [15-24] and low and high flux plasma exposure [16, 22-35] of single crystal or polycrystalline commercial tungsten grades (including grades produced specifically to comply with ITER specification) and W-based alloys. The application of NI allowed one to assess the local change of mechanical properties at the nano-scale (hardening or softening in the grain with a certain crystallographic orientation) due to the presence of radiation- or plasma-induced defects (i.e. dislocation loops, voids and subsurface bubbles) accumulated within a shallow depth, and correlate it with the available results of corresponding microstructural investigations such as transmission electron microscopy (TEM).

More recently, several works were dedicated to modelling of NI experiments in tungsten [36-41], which is needed to extract the physical properties of tungsten, to mature the NI measurement methodology and to interpret the experimental data. These works have already provided a considerable insight into the physics of NI process in tungsten, but all of them treat the experimental data obtained at room temperature only. However, due to its relatively high DBTT, tungsten will operate at elevated temperature, therefore the characterization of the plasma- and neutron-damage by NI will be needed at high temperature, i.e. at least at 473 K (the base temperature of W in ITER) and above. Besides, the above-cited simulation works have been based on either linear elastic (considering elastic regime solely) or the Peirce-Asaro-Needleman *crystal plasticity* constitutive laws [42]. However, the classical formulation of this model treats the critical resolved shear stress (CRSS) as a single state variable, which is a limitation when multiple deformation mechanisms are at play.

In the present paper, we extend the Peirce-Asaro-Needleman model by decomposing the CRSS into the different contributions accounting separately for the impact of lattice friction, dislocation forest hardening and dislocation grain boundary pinning (i.e. the Hall-Petch effect). In our model, each component depends on the temperature and actual microstructure of the material under investigation. Thus, we can account for the impact of the microstructural changes induced, e.g. by plasma exposure, heat shock or irradiation by energetic particles, including heavy ion irradiation which is known to produce strongly non-homogeneous damage profile.

In the very recent work, the indentation of tungsten done at the elevated temperature up to 1223 K has been reported [43]. However, the studies focused on T above 773 K and the hardness was calculated using a theoretical dependence of the contact area on the indentation depth. In this work, we present NI experiments carried out at room and elevated temperature, covering the range below 700 K down to room temperature. The results are treated by a crystal plasticity finite element method (CPFEM) model, which is applied to extract the constitutive law parameters in the temperature range of 300-691 K. The material plasticity parameters were identified by comparing the measured and predicted load–displacement curves and hardness data. To ensure the industrial relevance of this work, we carried out the experiments on the commercial tungsten grade of 99.97 weight % purity produced according to the ITER specification.

2. Methodology

2.1 Experimental procedure

The original bulk material has been supplied by Plansee AG as a bar with a 36x36 mm^2 square cross-section. The bar was fabricated by hammering on both sides. The grains had therefore the needle-like shape, as shown in Fig. 1(a). The samples for NI were cut to 20×20×1 mm^3 dimension and then annealed at 2073 K for one hour to remove any damage associated with the electric discharge machine cutting and to recrystallize the grains. As a result of this annealing, the scanning electron microscopy–electron backscatter diffraction (SEM–EBSD) analysis revealed that grains became equiaxed, and their mean size was 36 µm, as shown in Fig. 1(b). The initial dislocation density was about (4-8)×10^{12} m^{-2} and after the annealing it was reduced below 10^{10} m^{-2}, as it was revealed by TEM. Then the samples were grinded using 1200 grit paper and polished in 9 µm, 3 µm and 1µm grain size diamond suspensions, followed by a final polishing step using silica nanoparticles.

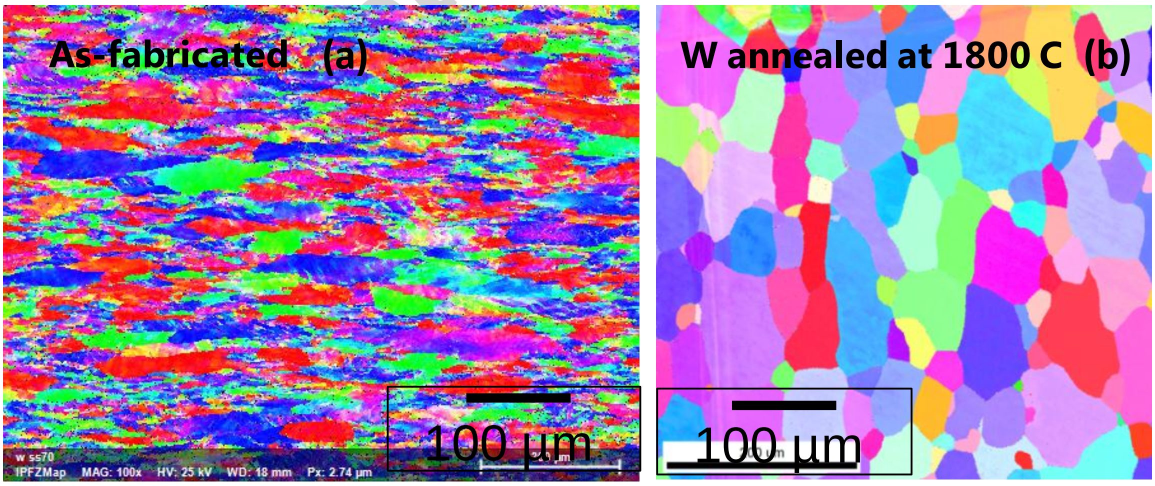

Fig. 1. SEM-EBSD inverse pole figure maps of (a) as-fabricated and (b) recrystallized tungsten.

NI has been performed in a High Temperature nano-mechanical testing system from Anton Paar (UNHT^3-HTV), which can record the load displacement curves and determine the hardness at several temperatures and indentation depths. The high temperature NI was carried out in vacuum using a tungsten carbide (WC) indenter tip mounted in a molybdenum shaft to which thermocouples have been welded. The UNHT indenter head is based on an active surface referencing system consisting of two probes (indenter and reference) in order to minimize the instrumental compliances and the thermal drift. A reference tip, made of a sapphire ball mounted in a similar shaft as the one supporting the WC indenter, was placed at a distance of 9.3 mm from the indenter tip. Heating was applied to the indenter tip, the reference tip and the sample, and in each case the temperature was controlled independently. To avoid the use of glues that may be an additional source of system compliances, the samples were held in a clamping stage by a retaining disc that fixed the sample to a highly thermal conductive graphite substrate. The heating was performed by infrared lamps placed below the graphite substrate. The temperature stabilization was achieved by equilibration of the thermal bath created between the two tips and the sample. Firstly, the probes and the sample were heated up to the target temperature and let stabilize in servo-loop mode while the sample surface was at 500 µm distance from the probes. Then, the temperature feedback control was switched off and the temperature of the reference probe was adjusted to match the sample temperature by bringing it into contact with the sample and minimizing the temperature change. Then the temperature of the indenter probe was matched with the sample temperature by fine tuning the power of the infrared lamp while performing a long indentation (5 min at F_{max}, and 5 min at 10% of F_{max}). This procedure allowed one to achieve the thermal drifts below 20 nm/min in all measurements. The thermal drift was determined in between measurements by the change in displacement after unloading to 10 % of F_{max}. After the temperature equilibration a set of single cycle NI were carried out in force control mode up to 50 mN and 100 mN of maximum load, F_{max} . 3 to 6 standard measurements were performed for each condition using loading and unloading times of 30 s, a dwell time of 10 s and spacing between indents of 50 µm. The test temperature was considered to be the temperature measured at the indenter tip, i.e. 122 ± 1 °C, 232 ± 2 °C and 418 ± 2 °C. The indentation hardness values were estimated using the classical Oliver & Pharr method [44] and fitting a power law to the first segment of the unloading curve (from 98% to 40%) [44]. The tip area function and the frame compliance were calibrated by an iterative approach performing a series of indents in two reference materials: used silica and tungsten, as described in [45], using Poisson's ratio of 0.24 and elastic modulus of 700 GPa for the indenter material, WC. The frame compliance amounted to 0.51 nm/mN. The zero contact point was set using a contact stiffness threshold of 800 µN/µm.

2.2 CPFEM for the NI of tungsten

In this work, the CPFEM is applied to simulate the NI process in the temperature range of 300-691 K, following the available experimental data. In the next subsections, the single crystal plasticity theory with temperature effect is firstly introduced. Then, the detailed information is presented for the setup of the finite element model.

2.2.1 Single crystal plasticity theory

Within the framework of classical crystal plasticity theory [46], the deformation of materials can be divided into the elastic and plastic stages. Plastic deformation is dominated by the dislocation motion in slip systems. The viscoplastic strain rate related to the dislocation glide can be given as

$$\dot{\varepsilon}^{\mathrm{vp}} = \sum_{\alpha=1}^{N_{\mathrm{s}}} \mathbf{R}^{\alpha} \dot{\gamma}^{\alpha} \tag{1}$$

where N_{s} and $\mathbf{R}^{\alpha}$ are respectively the number of slip systems and the Schmid factor. $\mathbf{R}^{\alpha} = \frac{1}{2}(\mathbf{s}^{\alpha} \otimes \mathbf{n}^{\alpha} + \mathbf{n}^{\alpha} \otimes \mathbf{s}^{\alpha})$ with $\mathbf{s}^{\alpha}$ and $\mathbf{n}^{\alpha}$ representing the unit vectors for the slipping and normal direction of the α-th slip system, respectively. For each slip system, the corresponding plastic shear rate can be defined as

$$\dot{\gamma}^{\alpha} = \dot{\gamma}_0 \left| \frac{\tau_{\mathrm{RSS}}^{\alpha}}{\tau_{\mathrm{CRSS}}^{\alpha}} \right|^{\frac{1}{m}} \mathrm{sgn}(\tau_{\mathrm{RSS}}^{\alpha}) \tag{2}$$

where $\dot{\gamma}_0$ and m are, respectively, the reference shearing rate and strain rate sensitivity. $\tau_{\mathrm{RSS}}^{\alpha}$ is the resolved shear stress, and $\tau_{\mathrm{CRSS}}^{\alpha}$ is the CRSS. Concerning the plastic deformation of polycrystalline tungsten, three hardening mechanisms should be taken into account at intermediate temperatures, therefore, $\tau_{\mathrm{CRSS}}^{\alpha}$ is expressed as follows:

$$\tau_{\mathrm{CRSS}}^{\alpha}(T) = \tau_{\mathrm{LF}}(T) + \tau_{\mathrm{HP}}(T) + \tau_{\mathrm{SSD}}^{\alpha}(T) \tag{3}$$

where τ_{LF}, τ_{HP} and $\tau_{\mathrm{SSD}}^{\alpha}$ are, respectively, the lattice friction stress, Hall-Petch hardening and dislocation hardening terms. The term τ_{HP} originates from piling-up of dislocations heading to grain boundaries, and the term $\tau_{\mathrm{SSD}}^{\alpha}$ is induced by the dislocation-dislocation interaction.

Plastic deformation in body-centered cubic (bcc) metals at intermediate temperature is well known to be mediated by the movement of screw dislocations, which is a thermally activated process. Following the work of Lim et al. [47], the lattice friction stress τ_{LF} can be expressed as:

$$\tau_{\mathrm{LF}}(T)=\begin{cases}\tau_{\mathrm{p0}}\left[1-\sqrt{\dfrac{k_{\mathrm{B}}T}{2H_{\mathrm{k}}}\ln\left(\dfrac{\dot{\gamma}_{\mathrm{p0}}}{\dot{\varepsilon}}\right)}\right],T\le T_0\\ \tau_{\mathrm{f0}}\left[1-\dfrac{k_{\mathrm{B}}T}{2H_{\mathrm{k}}}\ln\left(\dfrac{\dot{\gamma}_{\mathrm{p0}}}{\dot{\varepsilon}}\right)\right]^2,T>T_0\end{cases}\tag{4}$$

where τ_{p0} and τ_{f0} are the reference stresses for the screw dislocations below and above T_0, respectively. k_{B} is the Boltzmann constant and $2H_{\mathrm{k}}$ is the formation enthalpy of the kink pair on a screw dislocation. $\dot{\gamma}_{\mathrm{p0}}$ and T_0 are the reference strain rate and the critical temperature, which separates the elastic interaction and the line tension regimes. $\dot{\varepsilon}$ is the loading strain rate. For the case of NI, $\dot{\varepsilon}$ can be defined as [48]

$$\dot{\varepsilon}=\frac{1}{h}\frac{\mathrm{d}h}{\mathrm{d}t}\tag{5}$$

where h is the indentation depth.

Following the Hall-Petch relationship [49], τ_{HP} is related to the Hall-Petch coefficient k_{HP} and average grain size d in the following way:

$$\tau_{\mathrm{HP}}(T)=k_{\mathrm{HP}}(T)d^{-0.5}\tag{6}$$

The value of k_{HP} tends to decrease with the increase of temperature due to the thermally-activated interaction of dislocations with grain boundaries and facilitated absorption of dislocations into the grain boundary interfaces.

The dislocation interaction and multiplication also result in the material strengthening, and $\tau_{\mathrm{SSD}}^{\alpha}$ can be expressed as:

$$\tau_{\mathrm{SSD}}^{\alpha}(T)=\mu(T)bh_{\mathrm{SSD}}(T)\sqrt{\rho_{\mathrm{SSD}}^{\alpha}}\tag{7}$$

where $\mu(T)=\sqrt{[C_{11}(T)-C_{12}(T)]C_{44}(T)/2}$ is the temperature-dependent shear modulus, and the elastic constants C_{ij} for tungsten can be found in [50]. h_{SSD} is the dislocation strength coefficient, which is assumed to decrease linearly with temperature i.e. $h_{\mathrm{SSD}}(T)=h_{\mathrm{SSD}}^0-k_{\mathrm{SSD}}T$ following the earlier study [51]. b and $\rho_{\mathrm{SSD}}^{\alpha}$ are the magnitude of the Burgers vector and the density of statistically stored dislocations (SSDs), respectively.

As the plastic deformation progresses, the generation of SSDs within the plasticity affected region would result in the evolution of the CRSS, i.e.

$$\dot{\tau}_{\mathrm{CRSS}}^{\alpha}(T)=\sum_{\beta=1}^{N_s} H^{\alpha\beta}(T)\,|\dot{\gamma}^{\beta}| \tag{8}$$

where the hardening matrix $H^{\alpha\beta}$ can be expressed as [52]

$$H^{\alpha\beta}(T)=\alpha_0\left|1-\frac{\tau_{\mathrm{SSD}}^{\beta}(T)}{\tau_{\mathrm{SSD}}^{\max}}\right|^{n_0} m^{\alpha\beta} \tag{9}$$

where α_0 and n_0 are the dislocation hardening coefficient and the dislocation interaction sensitivity coefficient, respectively. $m^{\alpha\beta}$ is the matrix indicating the interaction strength between dislocations gliding in slip systems α and β [52]. $\tau_{\mathrm{SSD}}^{\max}$ denotes the maximum SSD hardening strength when the density of SSDs gets saturated.

2.2.2 Finite element method model setup

In this work, the theoretical model developed in the previous subsection is applied to simulate the NI of tungsten at elevated temperatures with the Berkovich indenter. The constitutive equations are implemented into the subroutine VUMAT of Abaqus. The sample is taken as a cylinder with the height of 20 μm and radius of 20 μm as illustrated in Fig. 2(a). The meshed elements for the sample and Berkovich indenter are shown in Fig. 2(b). The sample contains 22848 linear hexahedral elements of type C3D8R and 24344 nodes, and the Berkovich indenter is taken as a rigid body meshed with R3D4 and R3D3 elements. For the region beneath the indenter tip, the mesh is refined with the minimum size of 0.1 μm and 0.25 μm along the z axis direction and in the x-y plane, respectively. The bottom of the sample is fixed, and the rest surfaces are free of constraints. The interaction between the sample surface and indenter tip is set as frictionless as it has a little effect on the force-depth relationship [53].

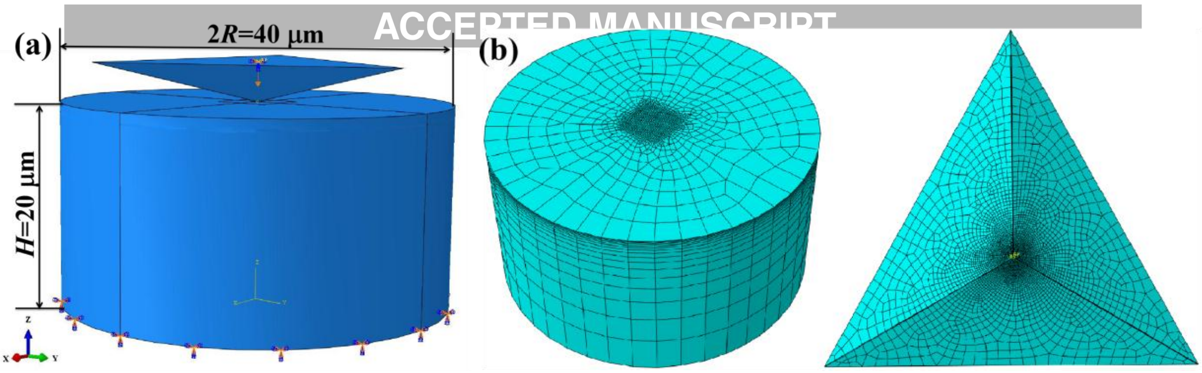

Fig. 2. (a) Schematic of the geometrical model for the NI of tungsten with a Berkovich indenter. The indented sample is taken as a cylinder with the height of 20 μm and radius of 20 μm. (b) The meshes of the sample and the Berkovich indenter with the tip radius 100 nm.

The temperature-dependent elastic constants for tungsten are taken from Ref. [50]. $N_s = 24$ represents the slip systems of $\{1\bar{1}0\}<111>$ and $\{11\bar{2}\}<111>$ types. The average grain size is taken as $d = 36$ μm, which was measured by the EBSD software. $h_{SSD}(T) = h_{SSD}^0 - k_{SSD}T$ with $h_{SSD}^0 = 0.38$ and $k_{SSD} = 4\times10^{-4}$ K^{-1} [51]. The initial and saturated density of SSD are taken to be 1×10^{10} m^{-2} and 1×10^{15} m^{-2}, respectively. In the experiment, the loading velocity was calculated to amount $\mathrm{d}h/\mathrm{d}t = 20$ nm/s at the beginning of the dwelling time. Therefore, the equivalent strain rate can be estimated as 0.02 s^{-1} following Eq. (5) when the indentation depth ranges from 500 nm to 1500 nm. The rest of parameters used in the simulation are listed in Table 1.

Table 1. Parameters of the constitutive law of tungsten

Variable	Value	Unit	Used in	Reference
$\dot{\gamma}_0$	0.001	s^{-1}	Eq. (2)	[51]
m	0.05	-	Eq. (2)	[51]
τ_{p0}	1038	MPa	Eq. (4)	[47]
τ_{f0}	2035	MPa	Eq. (4)	[47]
T_0	580	K	Eq. (4)	[47]
k_B	1.38×10^{-23}	J/K	Eq. (4)	[47]
H_k	1.65×10^{-19}	J	Eq. (4)	[47]
$\dot{\gamma}_{p0}$	3.71×10^{10}	s^{-1}	Eq. (4)	[47]

α_0	165	MPa	Eq. (9)	Fitted
n_0	4.0	-	Eq. (9)	Fitted

3. Results

3.1 Force-depth and hardness-depth relationship

In this subsection, the proposed CPFEM model is applied to simulate the NI of recrystallized tungsten at room and high temperature. According to the crystal orientation map of the recrystallized tungsten, obtained with the help of EBSD (Fig. 1(b)), crystallographic orientations [111], [101] and [212] are dominant, representing 15%, 20% and 65% of the total explored area, respectively. Therefore, simulations were performed for the three crystallographic orientations for every considered value of temperature, and the final force-depth relationship for polycrystalline tungsten is obtained as a weighted sum of the force-depth curves corresponding to the three loading directions. The contribution of the lattice friction and dislocation hardening terms was established earlier in a wide temperature range [51]. Thus, the Hall-Petch hardening contribution is the only parameter that was varied to fit the simulation results to the experimental force-depth curves at different temperatures. The best match (as illustrated in Fig. 3) was achieved if τ_{HP} is taken to be 620 MPa, 486 MPa, 335 MPa and 245 MPa at 300 K, 395 K, 505 K and 691 K, respectively. With the increase of temperature, the loading force decreases at the same indentation depth, which indicates the material softening at high temperatures. The softening is attributed to the enhanced plasticity as the strength of the dislocation-dislocation and dislocation-grain boundary interaction decreases.

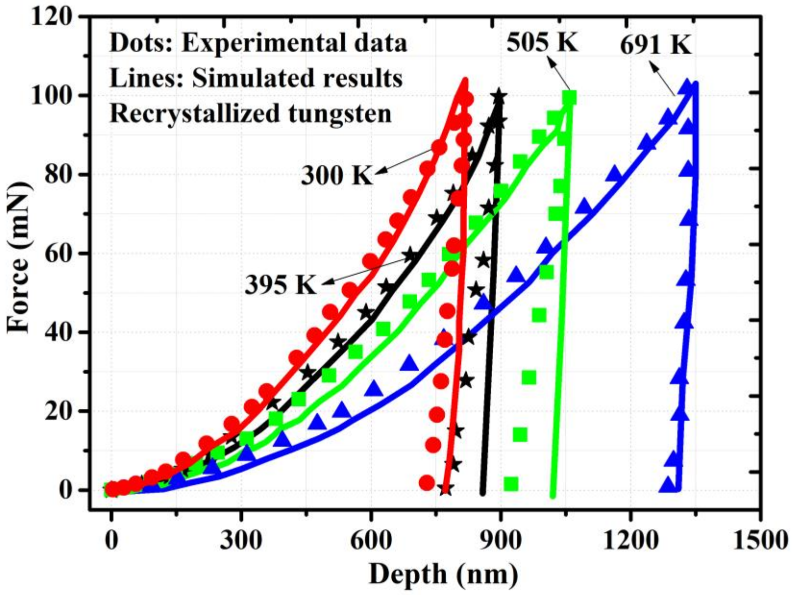

Fig. 3. The simulated (lines) and experimental (symbols) force-depth relationships for recrystallized W at 300 K, 395 K, 505 K and 691 K.

Based on the force-depth relationship, the indentation hardness can be calculated as $H = F / A$ where F and A are the load and contact area, respectively [44]. For the Berkovich indenter, the contact area A is defined as $A = 24.56 h_{c}^{2}$ where $h_{c} = h - k \cdot F / (\mathrm{d}F / \mathrm{d}h)$ and $k = 0.75$ [44]. Fig. 4 illustrates the calculated hardness-depth relationships at different temperatures, which are compared with the experimental data. One can see that a good agreement is achieved. The hardness decreases from ~6 GPa at the room temperature down to 2 GPa at 691 K, which is consistent with the evolution of the force-depth relationships, as shown in Fig.3. It should be noted that the indentation size effect is not obvious when the indentation depth is larger than 500 nm, therefore, the contribution of geometrically necessary dislocations is not covered in this simulation work, and the simulated hardness is a constant value for a given temperature.

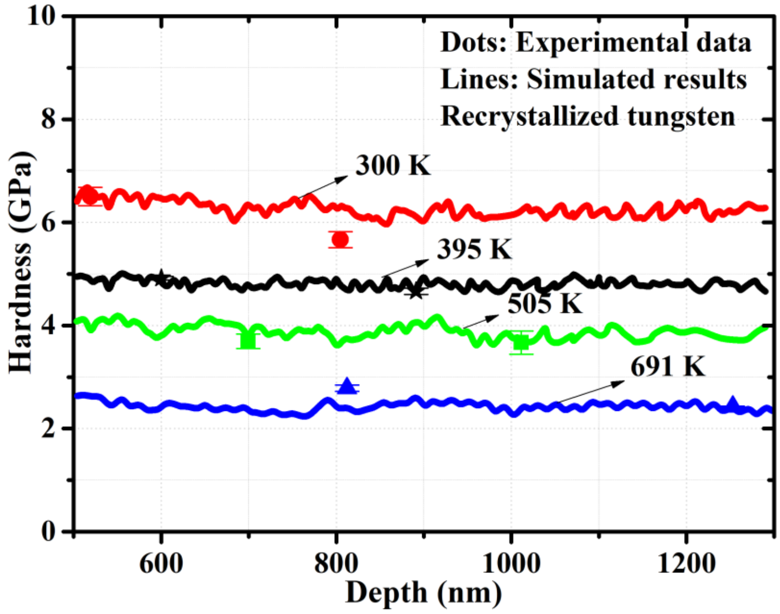

Fig. 4. The simulated (lines) and experimental (symbols) hardness-depth relationships for recrystallized W at 300 K, 395 K, 505 K and 691 K. Note that the hardness calculated from the experimental loading curves is obtained by using the relationship for the area A(h) derived from the calibration measurements.

3.2 Comparison of lattice friction and Hall-Petch hardening terms

Fig. 5 illustrates the temperature dependency of the CRSS components, namely, the lattice friction, Hall-Petch effect and their sum. The lattice friction is calculated by Eq. (4), assuming the equivalent strain rate of 0.02 s^{-1}. It can be seen that: (1) Both the lattice friction and Hall-Petch contribution decrease with the increase of temperature, as expected given their temperature-dependent features. (2) The Hall-Petch contribution is larger than that of lattice friction in the whole tested temperature range, indicating that the Hall-Petch effect is the dominant hardening mechanism for the recrystallized tungsten. Given that the average grain size of the studied tungsten is 36 μm, the Hall-Petch coefficient can be evaluated from the corresponding values of τ_{HP} reported in Section 3.1 as 3.72, 2.92, 2.01 and 1.47 MPa·m$^{0.5}$ at 300 K, 395 K, 505 K and 691 K, respectively (as shown in Fig. 6). Note that its value obtained at room temperature (3.72 MPa·m$^{0.5}$) is close to the result (3.1 MPa·m$^{0.5}$) of another independent study [54]. Besides, the values of the Hall-Petch coefficient k_{HP} and dislocation strength coefficient h_{SSD}, calculated in our previous work for higher temperature [51] are added in Fig. 6. With increasing the test temperature, the Hall-

Petch coefficient strongly decreases in the interval 500-800 K from ~2 MPa·m$^{0.5}$ to 0.45 MPa·m$^{0.5}$, which correlates very well with the range of the DBTT for this tungsten grade.

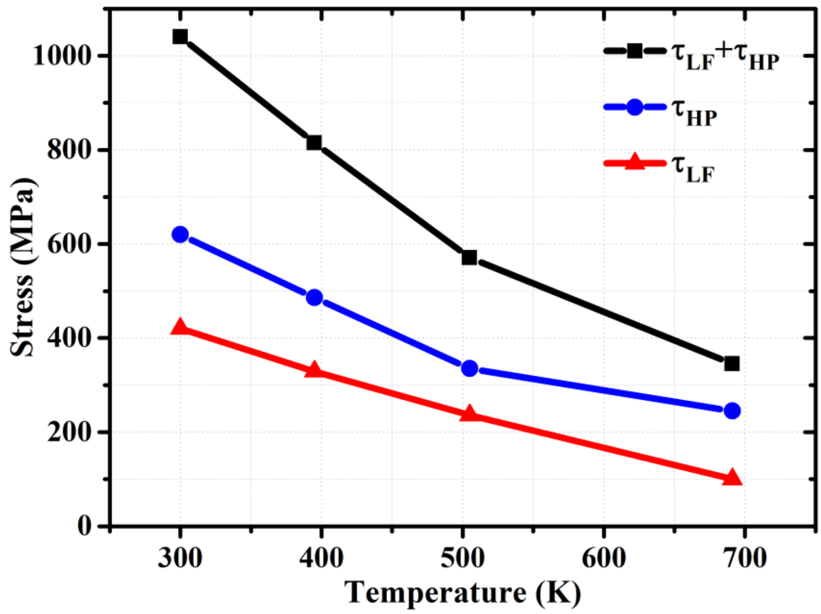

Fig. 5. The temperature evolution of the lattice friction, the Hall-Petch effect and their sum revealed with the help of CPFEM.

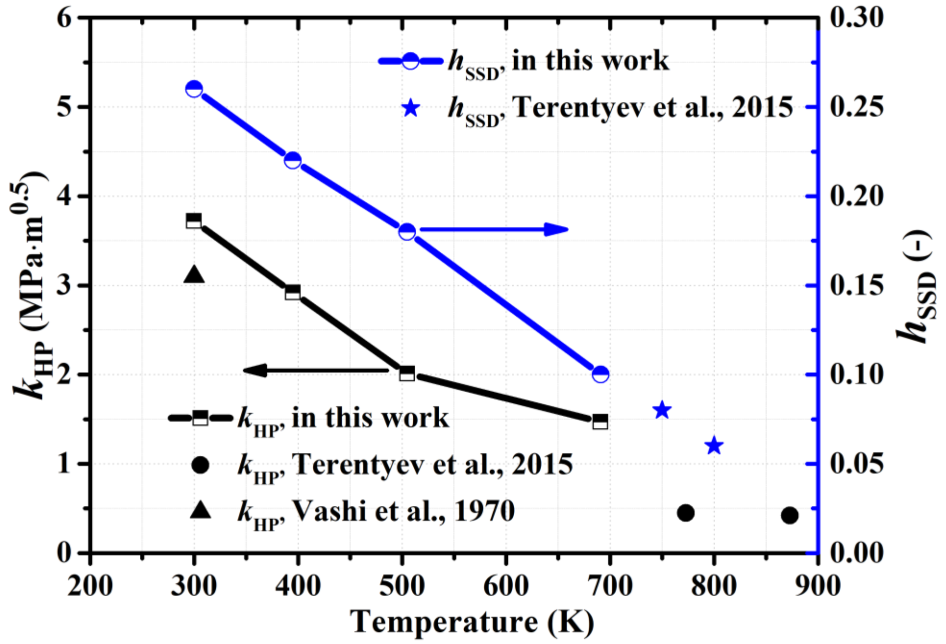

Fig. 6. Temperature dependency of the Hall-Petch coefficient and the dislocation strength coefficient.

3.3 Distribution of PEEQ, Von Mises stresses and τ_{SSD}^{1}

In order to understand the details of the NI process and estimate the size of the plasticity affected region in the performed FEM simulations, the distribution of equivalent plastic strain (denoted as PEEQ in Abaqus) beneath the indenter tip is analyzed at every studied temperature. The indentation depth is 750 nm, and the loading direction is [212]. We approximate the plasticity affected region as a hemisphere with radius R, which linearly increases with the indentation depth h with ratio M ($R=M\cdot h$). As illustrated in Fig. 7, R slightly increases with temperature, which can be attributed to the reduction of the yield stress with the increase of temperature promoting the extension of the plasticity affected region. The ratio M as a function of temperature is presented in Fig. 8(a), which linearly raises from 5.3 to 7.1 with the temperature increasing from 300 K up to 691 K. To clarify how M varies depending on the penetration depth, it was calculated for different depths for the two limiting values of test temperature. The results are presented in Fig. 8(b), which shows that M is almost a constant in the range of indentation depth 350-700 nm.

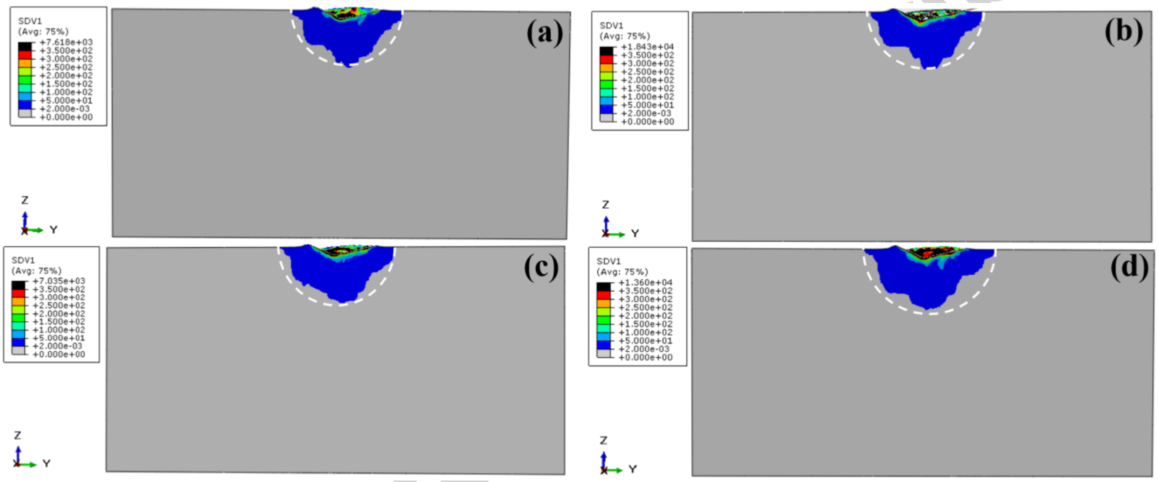

Fig. 7. Distribution of the equivalent plastic strain (PEEQ) at (a) 300 K, (b) 395 K, (c) 505 K and (d) 691 K. The indentation depth is 750 nm, and the loading direction is [212].

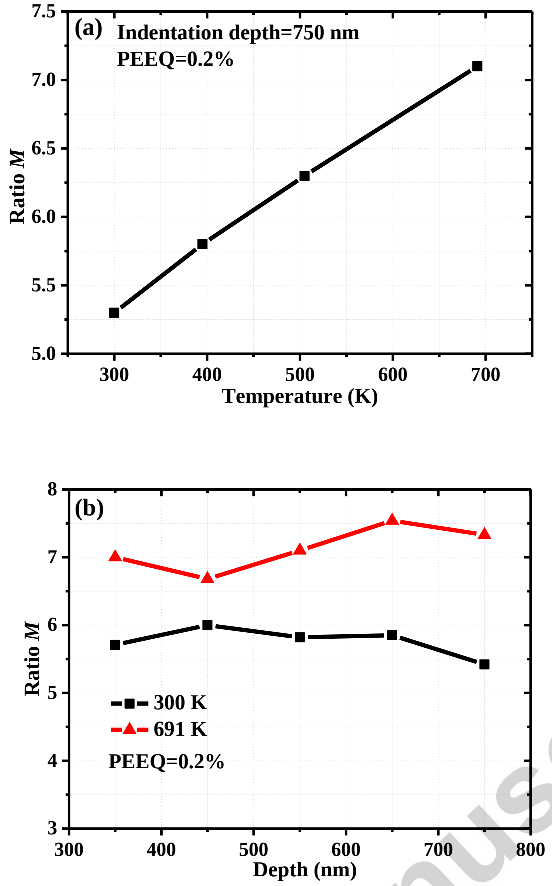

Fig. 8. (a) Ratio *M* as a function of the test temperature. Indentation depth is 750 nm. (b) Ratio *M* as a function of the indentation depth at 300 K and 691 K. Indentation along the crystallographic direction [212].

Fig. 9 presents the distribution of the von Mises stress when the indentation depth is 750 nm, and the loading direction is [212]. In accordance with the distribution of PEEQ, the region of high von Mises stress gradually shrinks with the increase of the test temperature, which is explained by the temperature-enhanced plasticity. Furthermore, the distribution of the dislocation hardening term in slip system $(\bar{1}11)[110]$ (i.e. τ^{1}_{SSD}) is shown Fig. 10. Comparing Figs. 9 and 10, one can see that the magnitude of τ^{1}_{SSD} is one order of magnitude lower than that of the von Mises stress. This means that the dominant contribution to the resistance of recrystallized tungsten against the indenter penetration comes from the lattice friction and Hall-Petch effect.

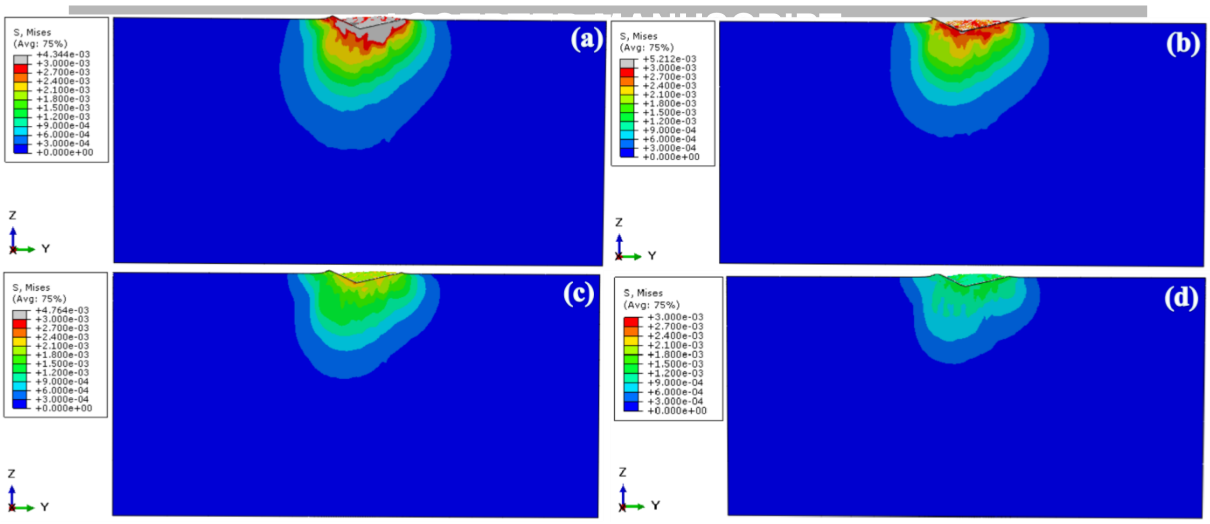

Fig. 9. Distribution of the von Mises stress (measured in TPa) at (a) 300 K, (b) 395 K, (c) 505 K and (d) 691 K. The indentation depth is 750 nm, and the loading direction is [212].

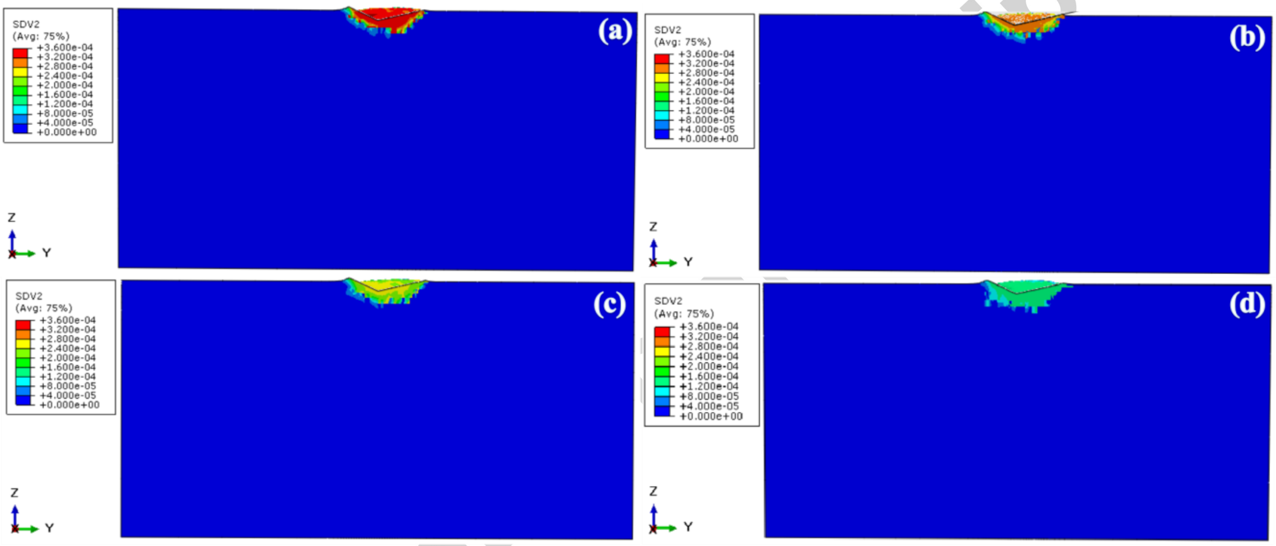

Fig. 10. Distribution of τ^{1}_{SSD} (measured in TPa) at (a) 300 K, (b) 395 K, (c) 505 K and (d) 691 K . The superscript “1” indicates the slip system $(1\bar{1}1)[110]$. The indentation depth is 750 nm, and the loading direction is [212].

4. Summary and conclusions

We have performed the NI measurements on the commercially pure tungsten which was recrystallized to get large equiaxed grains (thus to avoid the effect of texture, which would complicate the modelling approach). The experimental results have demonstrated that the saturated nanohardness decreases almost linearly with increasing the test temperature from 6 GPa at room temperature down to 2 GPa at 691 K.

The CPFEM tool was applied to simulate the indenter penetration, and an iterative procedure was used to derive a number of physical parameters determining the plastic deformation in the material. As a result, we have obtained the lattice friction stress, dislocation-dislocation and dislocation-grain boundary interaction strengths in the temperature range below and around the DBTT i.e. 300-691 K. The knowledge of these parameters allows one to derive the constitutive law to describe the plastic deformation of a representative volume element, which subsequently can be used in the coarse grain models to predict the response of tungsten and tungsten-based materials to thermo-mechanical loads with the correct description of its behaviour not just above but also below the DBTT.

The derivation of the plasticity parameters has been performed with the minimum number of fitting parameters, thanks to the previous works [51], which provided the temperature dependence for the lattice friction and dislocation-dislocation interaction strength. Correspondingly, we have extrapolated some of the plastic parameters from earlier works [51] and calculated the lattice friction stress using the highly reliable information from the *ab initio* calculations (such as the activation energy for the screw dislocation motion taken as 1.65 eV following the literature data [47]). Hence, the Hall-Petch strength coefficient was therefore the sole fitting parameter in the present study. It was found that the Hall-Petch strength decreases with increasing temperature (varied from 300 to 691 K) from 3.72 down to 1.47 $MPa \cdot m^{0.5}$. The dislocation strength parameter can be well approximated by the linear regression function as $0.38\text{-}4\times10^{-4}\cdot T$ [K].

Finally, the plastic strain and stress distributions during the indentation process were extracted from the CPFEM model to investigate the extension of the plasticity affected region underneath the indenter tip depending on the indentation temperature. The obtained results show that the plasticity affected region is larger than the penetration depth by a factor of 5.3 to 7.1, depending on the test temperature. This factor increases with the test temperature due to the progressive activation of slip systems. This information can be utilized to guide the future NI experiments to probe tungsten samples after exposure to heavy ions, which is an alternative approach to introduce the radiation damage and characterize the potential effect of neutron irradiation of the same dose.

Acknowledgements

The views and opinions expressed herein do not necessarily reflect those of the European Commission. Z. X. acknowledges the support by the National Nature Science foundation of China (NSFC) under Contract No. 11802344 and the initial funding provided by Central South University. J. R. C contribution has been supported by the EURATOM Direct Actions. This project has received funding from the Euratom research and training programme 2014-2018 under grant agreement No. 755039.

References

[1] G. Pintsuk, Tungsten as plasma facing material, Comprehensive Nuclear Materials 4 (2012) 551-581.
[2] M. Rieth, S.L. Dudarev, S.M.G. de Vicente, J. Aktaa, T. Ahlgren, S. Autusch, D.E.J. Armstrong, M. Balden, N. Baluc, M.F. Barthe, W.W. Basuki, M. Battabyal, C.S. Becquart, D. Blagoeva, H. Boldyryeva, J. Brinkmann, M. Celino, L. Ciupinski, J.B. Correia, A. De Backer, C. Domain, E. Gaganidze, C. Garcia-Rosales, J. Gibson, M.R. Gilbert, S. Giusepponi, B. Gludovatzj, H. Greuner, K. Heinola, T. Hoschen, A. Hoffmann, N. Holstein, F. Koch, W. Krauss, H. Li, S. Lindig, J. Linke, C. Linsmeier, P. Lopez-Ruiz, H. Maier, J. Matejicek, T.P. Mishra, M. Muhammed, A. Munoz, M. Muzyk, K. Nordlund, D. Nguyen-Manh, J. Opschoor, N. Ordas, T. Palacios, G. Pintsuk, R. Pippan, J. Reiser, J. Riesch, S.G. Roberts, L. Romaner, M. Rosinski, M. Sanchez, W. Schulmeyer, H. Traxler, A. Urena, J.G. van der Laan, L. Veleva, S. Wahlberg, M. Walter, T. Weber, T. Weitkamp, S. Wurster, M.A. Yar, J.H. You, A. Zivelonghi, Recent progress in research on tungsten materials for nuclear fusion applications in Europe, Journal of Nuclear Materials 432(1-3) (2013) 482-500.
[3] S.J. Zinkle, Fusion materials science: Overview of challenges and recent progress, Physics of Plasmas 12(5) (2005).
[4] A. Giannattasio, Z. Yao, E. Tarleton, S.G. Roberts, Brittle-ductile transitions in polycrystalline tungsten, Philosophical Magazine 90(30) (2010) 3947-3959.
[5] A. Loarte, G. Saibene, R. Sartori, M. Becoulet, L. Horton, T. Eich, A. Herrmann, M. Laux, G. Matthews, S. Jachmich, N. Asakura, A. Chankin, A. Leonard, G. Porter, G. Federici, M. Shimada, M. Sugihara, G. Janeschitz, ELM energy and particle losses and their extrapolation to burning plasma experiments, Journal of Nuclear Materials 313 (2003) 962-966.
[6] D. Terentyev, G. De Temmerman, T.W. Morgan, Y. Zayachuk, K. Lambrinou, B. Minov, A. Dubinko, K. Bystrov, G. Van Oost, Effect of plastic deformation on deuterium retention and release in tungsten, Journal of Applied Physics 117(8) (2015).
[7] A. Dubinko, D. Terentyev, A. Bakaeva, T. Pardoen, M. Zibrov, T.W. Morgan, Effect of high flux plasma exposure on the micro-structural and -mechanical properties of ITER specification tungsten, Nuclear Instruments & Methods in Physics Research Section B-Beam Interactions with Materials and Atoms 393 (2017) 155-159.
[8] A. Dubinko, D. Terentyev, A. Bakaeva, M. Hernandez-Mayoral, G. De Temmerman, L. Buzi, J.M. Noterdaeme, B. Unterberg, Sub-surface microstructure of single and polycrystalline tungsten after high flux plasma exposure studied by TEM, Applied Surface Science 393 (2017) 330-339.
[9] X. Xiao, L. Yu, A hardening model for the cross-sectional nanoindentation of ion-irradiated materials, Journal of Nuclear Materials 511 (2018) 220-230.
[10] X. Xiao, L. Yu, Comparison of linear and square superposition hardening models for the surface nanoindentation of ion-irradiated materials, Journal of Nuclear Materials 503 (2018) 110-115.
[11] X. Xiao, Q. Chen, H. Yang, H. Duan, J. Qu, A mechanistic model for depth-dependent hardness of ion irradiated metals, Journal of Nuclear Materials 485 (2017) 80-89.
[12] S.L. Huang, G. Ran, P.H. Lei, N.J. Chen, S.H. Wu, N. Li, Q. Shen, Effect of crystal orientation on hardness of He+ ion irradiated tungsten, Nuclear Instruments & Methods in Physics Research Section B-Beam Interactions with Materials and Atoms 406 (2017) 585-590.

[13] K. Miyahara, S. Matsuoka, N. Nagashima, Nanoindentation measurement for a tungsten (001) single crystal, Jsme International Journal Series a-Solid Mechanics and Material Engineering 41(4) (1998) 562-568.
[14] J.H.A. Hagelaar, E. Bitzek, C.F.J. Flipse, P. Gumbsch, Atomistic simulations of the formation and destruction of nanoindentation contacts in tungsten, Physical Review B 73(4) (2006).
[15] O. El-Atwani, J.S. Weaver, E. Esquivel, M. Efe, M.R. Chancey, Y.Q. Wang, S.A. Maloy, N. Mara, Nanohardness measurements of heavy ion irradiated coarse- and nanocrystalline-grained tungsten at room and high temperature, Journal of Nuclear Materials 509 (2018) 276-284.
[16] J.S. Weaver, C. Sun, Y.Q. Wang, S.R. Kalidindi, R.P. Doerner, N.A. Mara, S. Pathak, Quantifying the mechanical effects of He, W and He plus W ion irradiation on tungsten with spherical nanoindentation, Journal of Materials Science 53(7) (2018) 5296-5316.
[17] E. Hasenhuetl, Z.X. Zhang, K. Yabuuchi, A. Kimura, Effect of displacement damage level on the ion-irradiation affected zone evolution in W single crystals, Journal of Nuclear Materials 495 (2017) 314-321.
[18] E. Hasenhuetl, Z.X. Zhang, K. Yabuuchi, P. Song, A. Kimura, Crystal orientation dependence of ion-irradiation hardening in pure tungsten, Nuclear Instruments & Methods in Physics Research Section B-Beam Interactions with Materials and Atoms 397 (2017) 11-14.
[19] T. Hwang, M. Fukuda, S. Nogami, A. Hasegawa, H. Usami, K. Yabuuchi, K. Ozawa, H. Tanigawa, Effect of self-ion irradiation on hardening and microstructure of tungsten, Nuclear Materials and Energy 9 (2016) 430-435.
[20] A. Khan, R. Elliman, C. Corr, J.J.H. Lim, A. Forrest, P. Mummery, L.M. Evans, Effect of rhenium irradiations on the mechanical properties of tungsten for nuclear fusion applications, Journal of Nuclear Materials 477 (2016) 42-49.
[21] A. Xu, D.E.J. Armstrong, C. Beck, M.P. Moody, G.D.W. Smith, P.A.J. Bagot, S.G. Roberts, Ion-irradiation induced clustering in W-Re-Ta, W-Re and W-Ta alloys: An atom probe tomography and nanoindentation study, Acta Materialia 124 (2017) 71-78.
[22] D.E.J. Armstrong, T.B. Britton, Effect of dislocation density on improved radiation hardening resistance of nano-structured tungsten-rhenium, Materials Science and Engineering a-Structural Materials Properties Microstructure and Processing 611 (2014) 388-393.
[23] D.E.J. Armstrong, P.D. Edmondson, S.G. Roberts, Effects of sequential tungsten and helium ion implantation on nano-indentation hardness of tungsten, Applied Physics Letters 102(25) (2013).
[24] D.E.J. Armstrong, X. Yi, E.A. Marquis, S.G. Roberts, Hardening of self ion implanted tungsten and tungsten 5-wt% rhenium, Journal of Nuclear Materials 432(1-3) (2013) 428-436.
[25] W.Q. Chen, X.Y. Wang, X.Z. Xiao, S.L. Qu, Y.Z. Jia, W. Cui, X.Z. Cao, B. Xu, W. Liu, Characterization of dose dependent mechanical properties in helium implanted tungsten, Journal of Nuclear Materials 509 (2018) 260-266.
[26] S. Das, D.E.J. Armstrong, Y. Zayachuk, W. Liu, R. Xu, F. Hofmann, The effect of helium implantation on the deformation behaviour of tungsten: X-ray micro-diffraction and nanoindentation, Scripta Materialia 146 (2018) 335-339.
[27] M.Z. Zhao, F. Liu, Z.S. Yang, Q. Xu, F. Ding, X.C. Li, H.S. Zhou, G.N. Luo, Fluence dependence of helium ion irradiation effects on the microstructure and mechanical properties of tungsten, Nuclear Instruments & Methods in Physics Research Section B-Beam Interactions with Materials and Atoms 414 (2018) 121-125.
[28] M.H. Cui, T.L. Shen, H.P. Zhu, J. Wang, X.Z. Cao, P. Zhang, L.L. Pang, C.F. Yao, K.F. Wei, Y.B. Zhu, B.S. Li, J.R. Sun, N. Gao, X. Gao, H.P. Zhang, Y.B. Sheng, H.L. Chang, W.H. He, Z.G. Wang, Vacancy like defects and hardening of tungsten under irradiation with He ions at 800 degrees C, Fusion Engineering and Design 121 (2017) 313-318.
[29] J. Gibson, S.G. Roberts, D.E.J. Armstrong, High temperature indentation of helium-implanted tungsten, Materials Science and Engineering a-Structural Materials Properties Microstructure and Processing 625 (2015) 380-384.

[30] X. Ou, W. Anwand, R. Kogler, H.B. Zhou, A. Richter, The role of helium implantation induced vacancy defect on hardening of tungsten, Journal of Applied Physics 115(12) (2014).
[31] W.Z. Yao, P. Wang, A. Manhard, C.E. Krill, J.H. You, Effect of hydrogen on the slip resistance of tungsten single crystals, Materials Science and Engineering a-Structural Materials Properties Microstructure and Processing 559 (2013) 467-473.
[32] M.H. Cui, Z.G. Wang, L.L. Pang, T.L. Shen, C.F. Yao, B.S. Li, J.Y. Li, X.Z. Cao, P. Zhang, J.R. Sun, Y.B. Zhu, Y.F. Li, Y.B. Sheng, Temperature dependent defects evolution and hardening of tungsten induced by 200 keV He-ions, Nuclear Instruments & Methods in Physics Research Section B-Beam Interactions with Materials and Atoms 307 (2013) 507-511.
[33] X. Fang, A. Kreter, M. Rasinski, C. Kirchlechner, S. Brinckmann, C. Linsmeier, G. Dehm, Hydrogen embrittlement of tungsten induced by deuterium plasma: Insights from nanoindentation tests, Journal of Materials Research (2018).
[34] C.S. Corr, S. O'Ryan, C. Tanner, M. Thompson, J.E. Bradby, G.D. Temmerman, R.G. Elliman, P. Kluth, D. Riley, Mechanical properties of tungsten following rhenium ion and helium plasma exposure, Nuclear Materials and Energy 12 (2017) 1336-1341.
[35] D. Terentyev, A. Bakaeva, T. Pardoen, A. Favache, E.E. Zhurkin, Surface hardening induced by high flux plasma in tungsten revealed by nano-indentation, Journal of Nuclear Materials 476 (2016) 1-4.
[36] T. Volz, R. Schwaiger, J. Wang, S.M. Weygand, Numerical Study of Slip System Activity and Crystal Lattice Rotation under Wedge Nanoindents in Tungsten Single Crystals, 21st International ESAFORM Conference on Material Forming (ESAFORM), Univ Palermo, Palermo, ITALY, 2018.
[37] T. Volz, R. Schwaiger, J. Wang, S.M. Weygand, Iop, Comparison of three approaches to determine the projected area in contact from finite element Berkovich nanoindentation simulations in tungsten, 4th International Conference on Mechanical Engineering Research (ICMER), Kuantan, MALAYSIA, 2017.
[38] W.Z. Yao, C.E. Krill, B. Albinski, H.C. Schneider, J.H. You, Plastic material parameters and plastic anisotropy of tungsten single crystal: a spherical micro-indentation study, Journal of Materials Science 49(10) (2014) 3705-3715.
[39] W.Z. Yao, J.H. You, Berkovich nanoindentation study of monocrystalline tungsten: a crystal plasticity study of surface pile-up deformation, Philosophical Magazine 97(17) (2017) 1418-1435.
[40] L. Ma, D.J. Morris, S.L. Jennerjohn, D.F. Bahr, L.E. Levine, The role of probe shape on the initiation of metal plasticity in nanoindentation, Acta Materialia 60(12) (2012) 4729-4739.
[41] G.Y. Liu, M. Song, X.L. Liu, S. Ni, S.L. Wang, Y.H. He, Y. Liu, An investigation of the mechanical behaviors of micro-sized tungsten whiskers using nanoindentation, Materials Science and Engineering a-Structural Materials Properties Microstructure and Processing 594 (2014) 278-286.
[42] D. Peirce, R.J. Asaro, A. Needleman, An analysis of nonuniform and localized deformation in ductile single-crystals, Acta Metallurgica 30(6) (1982) 1087-1119.
[43] B.D. Beake, A.J. Harris, J. Moghal, D.E.J. Armstrong, Temperature dependence of strain rate sensitivity, indentation size effects and pile-up in polycrystalline tungsten from 25 to 950 degrees C, Materials & Design 156 (2018) 278-286.
[44] W.C. Oliver, G.M. Pharr, An improved technique for determining hardness and elastic-modulus using load and displacement sensing indentation experiments, Journal of Materials Research 7(6) (1992) 1564-1583.
[45] A. Ruiz-Moreno, P. Hahner, Indentation size effects of ferritic/martensitic steels: A comparative experimental and modelling study, Materials & Design 145 (2018) 168-180.
[46] R. Hill, J.R. Rice, Constitutive analysis of elastic-plastic crystals at arbitrary strain, Journal of the Mechanics and Physics of Solids 20(6) (1972) 401-413.
[47] H.J. Lim, C.C. Battaile, J.D. Carroll, B.L. Boyce, C.R. Weinberger, A physically based model of temperature and strain rate dependent yield in BCC metals: Implementation into crystal plasticity, Journal of the Mechanics and Physics of Solids 74 (2015) 80-96.

[48] Z.Q. Cao, X. Zhang, Nanoindentation stress-strain curves of plasma-enhanced chemical vapor deposited silicon oxide thin films, Thin Solid Films 516(8) (2008) 1941-1951.
[49] E.O. Hall, The Deformation and Ageing of Mild Steel: III Discussion of Results, Proceedings of the Physical Society. Section B 64 (1951) 747-753.
[50] R. Lowrie, A.M. Gonas, Single-crystal elastic properties of tungsten from 24^o to 1800^o C Journal of Applied Physics 38 (2004) 4505
[51] D. Terentyev, X.Z. Xiao, A. Dubinko, A. Bakaeva, H.L. Duan, Dislocation-mediated strain hardening in tungsten: Thermo-mechanical plasticity theory and experimental validation, Journal of the Mechanics and Physics of Solids 85 (2015) 1-15.
[52] A. Staroselsky, L. Anand, Inelastic deformation of polycrystalline face centered cubic materials by slip and twinning, Journal of the Mechanics and Physics of Solids 46(4) (1998) 671-696.
[53] Y. Wang, D. Raabe, C. Kluber, F. Roters, Orientation dependence of nanoindentation pile-up patterns and of nanoindentation microtextures in copper single crystals, Acta Materialia 52(8) (2004) 2229-2238.
[54] U.K. Vashi, R.W. Armstrong, G.E. Zima, The hardness and grain size of consolidated fine tungsten powder, Metallurgical Transactions 1 (1970) 1769-1771.